

Calibrating a Soft ERT-Based Tactile Sensor with a Multiphysics Model and Sim-to-real Transfer Learning

Hyosang Lee¹, Hyunkyu Park^{1,2}, Gokhan Serhat¹, Huanbo Sun³, and Katherine J. Kuchenbecker¹

Abstract—Tactile sensors based on electrical resistance tomography (ERT) have shown many advantages for implementing a soft and scalable whole-body robotic skin; however, calibration is challenging because pressure reconstruction is an ill-posed inverse problem. This paper introduces a method for calibrating soft ERT-based tactile sensors using sim-to-real transfer learning with a finite element multiphysics model. The model is composed of three simple models that together map contact pressure distributions to voltage measurements. We optimized the model parameters to reduce the gap between the simulation and reality. As a preliminary study, we discretized the sensing points into a 6 by 6 grid and synthesized single- and two-point contact datasets from the multiphysics model. We obtained another single-point dataset using the real sensor with the same contact location and force used in the simulation. Our new deep neural network architecture uses a de-noising network to capture the simulation-to-real gap and a reconstruction network to estimate contact force from voltage measurements. The proposed approach showed 82% hit rate for localization and 0.51 N of force estimation error performance in single-contact tests and 78.5% hit rate for localization and 5.0 N of force estimation error in two-point contact tests. We believe this new calibration method has the possibility to improve the sensing performance of ERT-based tactile sensors.

I. INTRODUCTION

Whole-body tactile sensors have received increasing attention because people want to use autonomous robots in unstructured environments where physical contact can occur at any location [1]. A biological skin-like compliance is beneficial to whole-body tactile sensors for many reasons including seamlessly covering complex geometries, absorbing external impacts, and conforming to the contact surface [2]. Nevertheless, creating soft and scalable tactile sensors is still challenging because deploying a large number of sensing elements requires robust, easy-to-manufacture, and reliable electrical connections across a compliant substrate [3].

Electrical resistance tomography (ERT) has shown many practical advantages for developing soft and scalable tactile sensors [4]–[9]. The ERT method reconstructs the continuous resistance distribution of an area surrounded by a relatively small number of electrodes. As shown in Fig. 1 (a), these

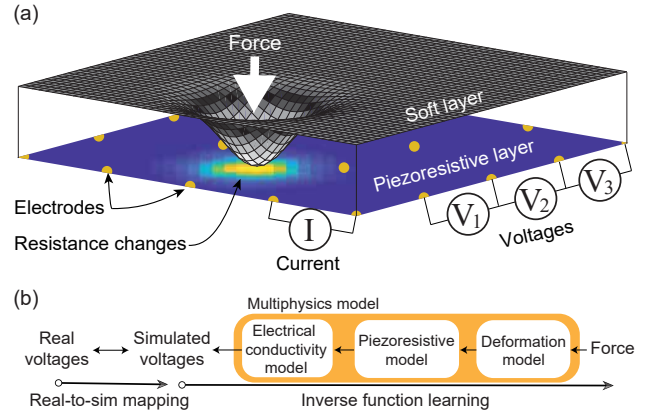


Fig. 1. (a) An illustration of the multiphysics model of our soft ERT-based tactile sensor containing a soft layer that lays on top of a piezoresistive layer and (b) a block diagram showing the proposed calibration framework.

electrodes are used to inject electrical current and to measure the corresponding voltages formed around the current pathway. An analytic conductivity model is typically used to calculate the resistance distribution from the applied electrical currents and corresponding measured voltages. This computational reconstruction technique helps simplify sensor fabrication [6] and enhance sensor robustness [10].

However, reconstructing the resistance distribution from a set of observed boundary voltage measurements is an ill-posed inverse problem [11]. Small errors in the voltage measurements can significantly distort the reconstructed resistance distribution. Moreover, the sensitivity of the reconstruction varies spatially [12]. Data-driven approaches have been actively adopted to improve the reconstruction performance of ERT-based tactile sensors by taking their intrinsic nonlinear behavior into account [13], [14]. Specifically, Martin and Choi [13] pursued a sim-to-real approach by using an electrical conductivity model to synthesize voltage data from randomized conductivity distributions. Similarly, Park et al. [14] improved the spatial resolution of an ERT-based tactile sensor using data from electrical conductivity simulation. They trained a deep neural network (DNN) using conductivity domain randomization and showed a generalized framework for improving the spatial resolution with which contacts can be detected.

In order to practically use ERT-based tactile sensors in real applications, the reconstructed resistance distribution should be calibrated to contact pressures. One possible approach is constructing an end-to-end mapping using indentation data [15], [16]. However, obtaining a well-generalized neural network is difficult in practice because acquiring sufficient

¹Hyosang Lee, Hyunkyu Park, Gokhan Serhat, and Katherine J. Kuchenbecker are with the Haptic Intelligence Department, Max Planck Institute for Intelligent Systems, 70569 Stuttgart, Germany {hslee, hkpark, serhat, kjk}@is.mpg.de

²Hyunkyu Park is also with the Department of Mechanical Engineering, Korea Advanced Institute of Science and Technology, 34141 Daejeon, South Korea hkpark93@kaist.ac.kr

³Huanbo Sun is with the Autonomous Learning Group, Max Planck Institute for Intelligent Systems, 72076 Tübingen, Germany huanbo.sun@tuebingen.mpg.de

real data requires an excessive amount of time. Another approach relies on using supervised learning to map the sensor signal to the imposed physical stimulation [17], [18]. Such sim-to-real transfer techniques have been widely adopted to resolve the data deficiency problem in many robotics applications, e.g., [19]–[21].

We hypothesize that a multiphysics model of an ERT-based tactile sensor can resolve this data deficiency problem because various conditions that cannot be easily tested in the real world can be extensively explored in simulation. This paper tests that hypothesis by introducing a method for calibrating soft ERT-based tactile sensors using two learning stages: real-to-sim mapping and inverse function learning. The mapping between the real and simulated voltages is established through supervised learning. The inverse function relating the voltages to the force is learned from data simulated by the developed multiphysics model, as shown in Fig. 1 (b).

II. A COMPUTATIONAL MULTIPHYSICS MODEL OF AN ERT-BASED TACTILE SENSOR

A. Conductive Fabric-based Tactile Sensor

We formulate a multiphysics model for the soft ERT-based tactile sensor that we previously constructed using neoprene and conductive fabric layers [5]. Fig. 2 (a) illustrates the structure of the sensor with five layers. The top layer is neoprene foam with a thickness of 4 mm. The next layer is an adhesive that glues the neoprene layer to the low-resistance fabric patches. The patches and a large sheet of high-resistance fabric form the piezoresistive layer; they are pressed together with no adhesive. Under the high-resistance fabric is a sheet of insulating fabric with a stitched circuit made of conductive thread. Twenty-four electrodes are connected to the high-resistance fabric through the stitched circuit.

The working principle of the piezoresistive layer is illustrated in Fig. 2 (b). The high-resistance fabric provides a base resistance between any two electrodes. When a force is applied to the neoprene, a corresponding compressive pressure is applied to the low-resistance fabric patches. From the compression, the contact resistance between the high-resistance fabric and the low-resistance patches decreases in the contact region.

B. Mechanical Deformation Model

The mechanical deformation of the sensor is calculated using a finite element (FE) model. This approach favors predicting the deformations accurately by realistically simulating the propagation and interaction of the structural stresses. The model is designed to be as simple as possible to capture the essential mechanics without inducing substantial computational cost. This model simplicity significantly influences the efficiency of generating simulation data.

The sensor is modeled including all five material layers shown in Fig. 2 (a). Although the real low-resistance patches have a discrete grid structure to prevent current from traveling between distant contacts, for simplicity their mechanical behavior is modeled as a continuous sheet similar to the other layers. For the computations, we use in-house

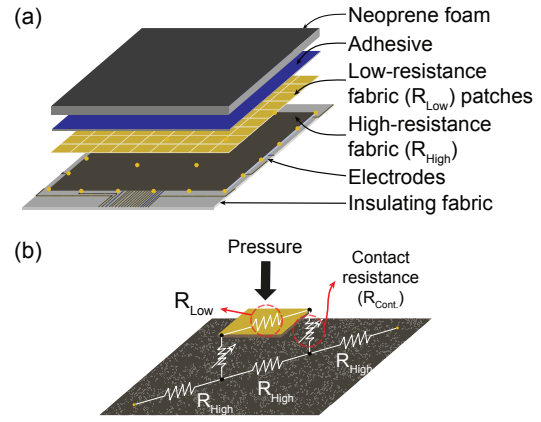


Fig. 2. (a) The piezoresistive structure using low-resistance fabric patches and high-resistance fabric and (b) the working principle of the piezoresistive structure.

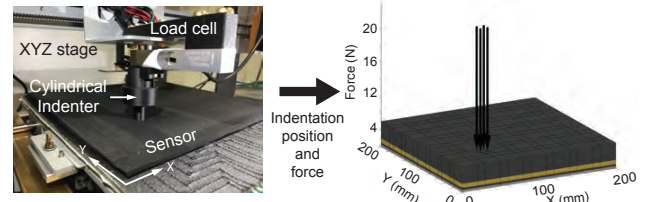


Fig. 3. The real indentation experimental setup (left) and the corresponding finite element deformation model in simulation (right).

FE analysis codes developed in MATLAB (Mathworks, USA) and based on linear elastic formulation. Each layer is discretized using 8-noded isoparametric brick elements that are assigned isotropic material properties. To increase the calculation accuracy, the FE mesh was designed with our predefined test points in mind. The nodes at the bottom of the sensor are fixed to the rigid support. Details of the adopted FE formulation are explained by Liu and Quek [22].

To enable supervised learning, the indentation experiments are simulated as shown in Fig. 3. In the real situation, the position of a cylindrical indenter with a diameter of 10 mm is precisely controlled by an XYZ stage. A load cell installed on the indenter measures the indentation force. The indentation position and force are identically imposed on the deformation model. In the simulations, four point forces are used instead of a single point force to account for the cylindrical geometry of the indenter. Fig. 3 (right) shows a schematic of the FE model subjected to indentation.

C. Piezoresistive Layer Model

The model of the piezoresistive layer was obtained from a specimen test as a look-up table. We prepared a specimen that can simply represent the working principle of the sensor. The specimen was located on a compressometer, and the entire surface was pressed several times while the force and resistance were measured simultaneously.

Figure 4 shows the relationship between the resistance and stress applied to the specimen. The result shows that the resistance monotonically decreases and begins to saturate as the stress increases over 0.02 MPa. During the cyclic compression test, a small hysteresis effect of 4.7% is observed between the loading and unloading curves. This value is

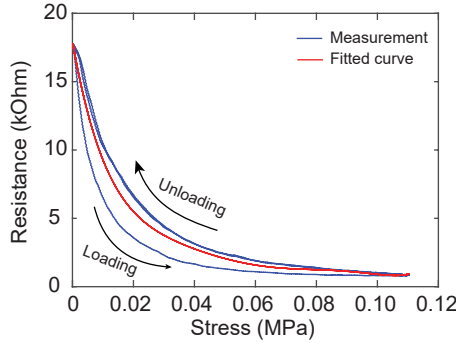


Fig. 4. The experimental result of the cyclic compression test.

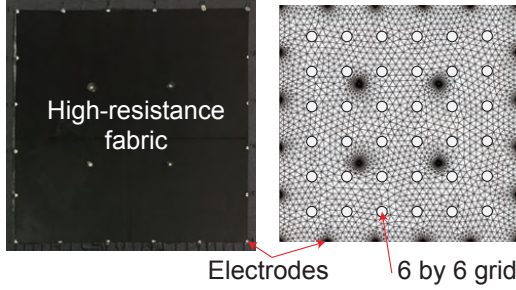


Fig. 5. A photographic image of the high-resistance fabric layer with 24 electrodes (left) and the finite element electrical conductivity model with identical geometry and electrodes (right). For reference, the 6 by 6 grid of predefined sensing points has been overlaid on the right image.

relatively small considering the compliance of the specimen. In this paper, we neglected the hysteresis effect and fitted the piezoresistive behavior as a fifth-order polynomial curve. In the multiphysics model, these polynomial coefficients are used to compute the sheet resistance change induced by the surface normal pressure between the high-resistance fabric layer and the low-resistance fabric layer. We assumed that the piezoresistive behavior is uniform across the entire sensor.

D. Electrical Conductivity Model

A finite element electrical conductivity model is used to calculate the voltages that are measured from the electrodes of the ERT-based tactile sensor. For a conductive domain (Ω) and its boundary ($\partial\Omega$), the continuum version of Kirchhoff's law describes the relationship between the boundary potential ϕ and conductivity distribution σ in the region Ω by assuming direct current and the absence of an interior current source.

$$\nabla \cdot (\sigma \nabla \phi) = 0 \text{ in } \Omega \quad (1)$$

The current density on the boundary is described as follows.

$$j = \sigma \nabla \phi \cdot \mathbf{n} \text{ in } \partial\Omega \quad (2)$$

where j is the current density and \mathbf{n} denotes the outward unit normal vector to $\partial\Omega$. We calculate voltages using equation (1) and (2) with the known conductivity distribution and current density at the boundary.

In the practical situation, current injection and voltage measurement are done through only a small number of electrodes. The sewn electrodes can contain a contact resistance between the high-resistance fabric and the electrode. This contact resistance reduces the voltage (V) measured from

the electrodes.

$$V = \phi + R\sigma \frac{\partial \phi}{\partial \mathbf{n}} \quad (3)$$

where R is the electrode contact resistance.

To solve equation (1) with boundary conditions, the conductive domain is discretized into finite elements. A weak formulation of equations (1) and (2) results in a system of linear equations. Details of a FE formulation of the conductivity model are explained by Holder et al. [11].

Fig. 5 shows the high-resistance fabric with 24 electrodes and the corresponding finite element model with the same geometry and electrode configuration. The resistance distribution of the finite element conductivity model is determined from the piezoresistive layer model. The voltages are measured from the full current injection pattern, which results in 6624 voltage measurements for our 24-electrode ERT system [5].

III. PARAMETER CHARACTERIZATION FOR THE MULTIPHYSICS MODEL

Although we limited the multiphysics model's complexity to keep the computational burden low, well-chosen model parameters can reduce the gap between simulation and reality. This section describes how parameters of the deformation model and the electrical conductivity model were chosen from experiments.

A. Indentation Experiment

The indentation setup shown in Fig. 3 (left) was used to gather calibration data. The XYZ stage moved the cylindrical indenter to the desired position and pressed it into the tactile sensor with a commanded indentation depth from 0 to 4 mm in 0.1 mm intervals. The indentation process was conducted in a quasi-static process. At each indentation step, the reaction force and voltages from the electrodes were stored at a rate of 2 Hz.

B. Determination of Mechanical Properties

The multi-layer model was calibrated by determining the layer material constants that result in accurate deformation values under applied forces. For each layer, two material parameters need to be determined: the elastic modulus (E) and Poisson's ratio (ν). The values of Poisson's ratio are taken from the literature. For the neoprene foam, it is selected as 0.3, which is a typical value for polymeric foams [23]. We assumed all the fabric to be lycra, so $\nu = 0.4$ is used, which is approximately the average of the values presented in the literature [24]. A polychloroprene-based adhesive is used as the glue chemical, which is nearly incompressible ($\nu = 0.495$) [23] and has a Young's modulus of 1.0 MPa.

The elastic moduli of neoprene (E_{neo}) and lycra fabric (E_{lyc}) are determined by minimizing the error between the indentation displacement values (e_{ind}) obtained through the indentation experiments and FE analyses. Since the indenter support is not perfectly firm, its stiffness (k_{ind}) is calculated by applying pseudo indentation on a rigid aluminum block

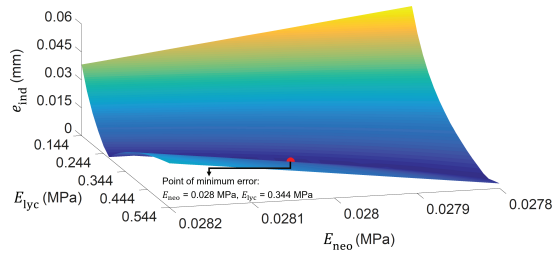


Fig. 6. The error surface of measured and simulated indentation depths as a function of E_{neo} and E_{lyc} .

TABLE I

THE MATERIAL PROPERTIES ASSIGNED TO THE FINITE ELEMENT MODEL.

Material	Young's modulus (MPa)	Poisson's ratio
Neoprene foam	0.028	0.300 [23]
Lycra fabric	0.344	0.400 [24]
Glue	1.000 [25]	0.495 [23]

and dividing the measured force value by the input displacement. Since the indenter and sensor are connected in series, the total stiffness of the setup (k_{tot}) satisfies the relation:

$$\frac{1}{k_{tot}} = \frac{1}{k_{ind}} + \frac{1}{k_{sen}} \quad (4)$$

where k_{sen} is the stiffness of the sensor. Finally, the experimental indentation depths are calculated by dividing the force values by k_{sen} . Fig. 6 shows the error surface of measured and simulated indentation depths as a function of E_{neo} and E_{lyc} . Table 1 presents the final material property values assigned to the FE model.

C. Electrode Contact Resistance Optimization

We characterized the 24 electrode contact resistances using an optimization method because these parameters are difficult to measure directly. The cost function was defined to be the L2-norm of the error between the measured voltages (V_{Real}) and the simulated voltages (V_{Sim}).

$$\underset{R_1 \dots R_{24}}{\operatorname{argmin}} \|V_{Real} - V_{Sim}\|_2 \quad (5)$$

where R_1 to R_{24} are the 24 electrode contact resistances. V_{Real} was obtained when the sensor was not compressed. The sheet resistance of the high-resistance fabric is known as 18 kOhm/square. Assuming homogeneous resistivity of the fabric, we can estimate the simulated voltages that correspond to the real situation. A direct searching method was used to find the best-fitting resistance values. Fig. 7 shows a comparison of V_{Real} and V_{Sim} from the initial guessed values of 10 Ohm (top) and with optimized electrode contact resistances (bottom). Modifying the electrode contact resistances reduces the estimation error.

D. Multiphysics Model Evaluation

The voltage changes (ΔV), which are the difference between the voltages (V) before and after the applied contact pressure distribution, are calculated from the multiphysics model in the same way as the voltage changes are measured in reality. For the evaluation of the multiphysics model, the

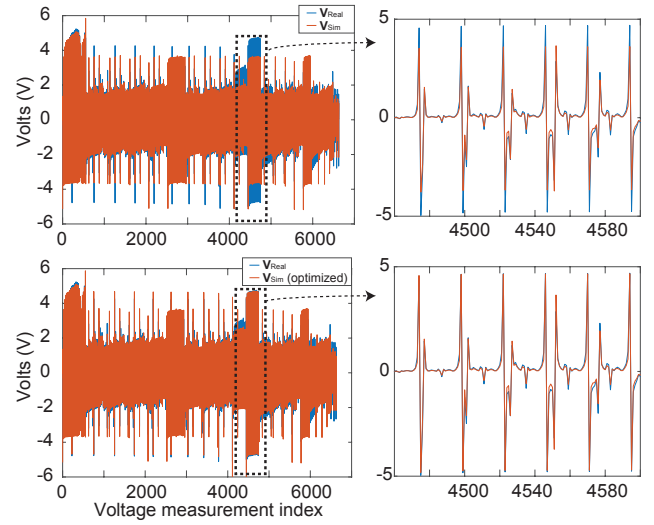


Fig. 7. The effect of the electrode contact resistance optimization. Each plot shows all 6624 voltage measurements needed for a single scan of the tactile sensor.

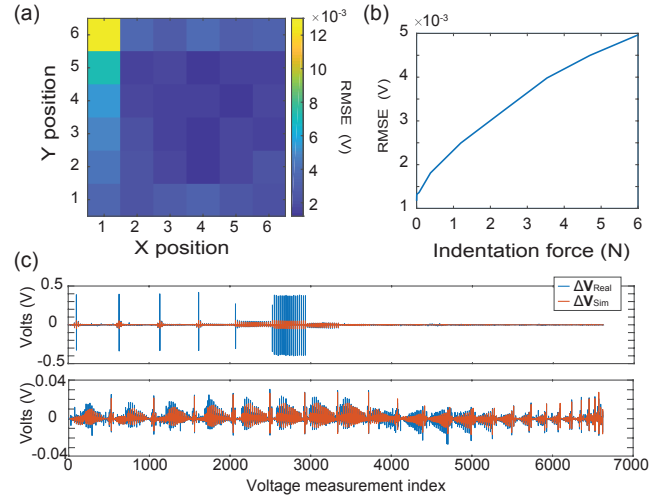


Fig. 8. (a) A heatmap of the RMSE of the voltage difference for the 6 by 6 grid locations, (b) the average RMSE of the voltage difference depending on the indentation force, and (c) two sample results from the location (1,6) showing the maximum error (top) and the location (4,3) showing the minimum error (bottom).

root mean square error (RMSE) of the voltage difference between ΔV_{Real} and ΔV_{Sim} is calculated using the data from the indentation experiment shown in Fig. 3. Each of the 6 by 6 grid locations shown in Fig. 5 (right) was indented up to 4 mm indentation depth.

Fig. 8 (a) shows the RMSE of the voltage difference depending on the contact location. The contact location on the left-top corner showed the highest error. We believe that the left-top area of the real sensor is more sensitive compared to the other areas due to fabrication inaccuracies.

Fig. 8 (b) shows the average RMSE of the voltage difference according to the indentation force. The estimation error tends to increase with the indentation force. This result implies that the model error tends to increase when deformations are large.

Fig. 8 (c) depicts the voltage readings with maximum and

minimum error. It is observed from the maximum error case that ΔV_{Real} is much larger than ΔV_{Sim} . This result means the resistance decreased more in the real situation compared to the simulation. But the multiphysics model captures the trends of the real voltage changes. The central area of the sensor tends to have less error, as shown in Fig. 8 (a). From the minimum error case, ΔV_{Real} seems to include unstructured noise and bias compared to ΔV_{Sim} , so we tried to close this simulation-to-real gap using learning.

IV. DNN MODEL FOR SIM-TO-REAL LEARNING

We used two DNNs (de-noising network, force estimation network) to improve the calibration performance of the tactile sensor. Even though we constrain the direction of the contact force to be along the surface normal, an enormous number of contact combinations is possible. As a preliminary study for this paper, we discretized the sensor domain into a 6 by 6 uniform grid and focused on contact localization and force estimation for one-point and two-point contact. The grid size was chosen to be similar to the number of electrodes, as this value theoretically limits the amount of meaningful information that can be extracted from the sensor [11].

A. DNN Architecture

We designed a novel architecture for high-performance calibration that consists of a de-noising network and a force estimation network (see Fig. 9). The de-noising network is a modified de-noising autoencoder (DAE) [26]. This network removes noise from real voltage measurements and fits the signals to the corresponding simulated voltage measurements. The force estimation network is designed to separately tackle localization and force estimation. This design constrains the number of contact points and helps the DNN model efficiently learn to estimate the force.

The force estimation proceeds in the following order. First, the location(s) of the contact(s) are identified from multi-label classification. In this stage, the result is a binary answer at each point in the 6 by 6 grid. The subsequent training estimates the force magnitude of the grid locations that were previously identified as having a contact.

The localization part has two layers each with 36 neurons and a sigmoid activation function. The output layer also uses a sigmoid activation function. The threshold of the sigmoid activation function was set to 0.5. The training was conducted with the binary cross-entropy loss function that is commonly used in multi-label classification [27].

The force estimation part has two layers with 36 neurons and a rectified linear unit (ReLU) function [28]. The ReLU activation was located at the end of the output layer based on the assumption that contact forces are always non-negative. The mean square error (MSE) was used as a loss function. Batch normalization was applied to all hidden layers for robust convergence during training. The outputs of the force estimation layer and localization layer are multiplied element-wise as a binary mask, so grid locations that are not identified from the localization layer always output an estimate of zero contact force.

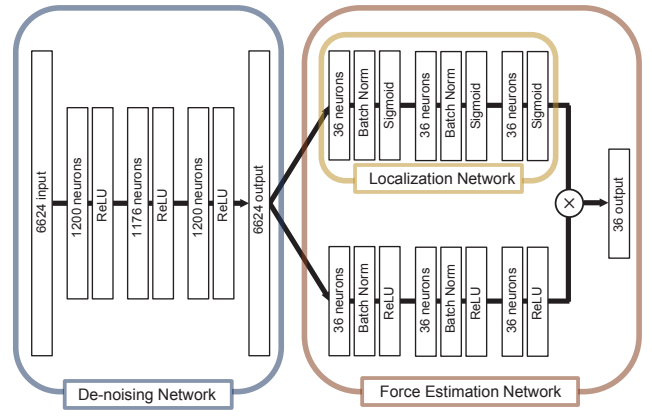


Fig. 9. A diagram of the DNN architecture for contact localization and force estimation.

B. Simulation Data Synthesis

For the force estimation network, the indentation experiment was simulated by virtually pressing every grid point. The indentation force was divided into 100 steps up to 10 N. All the possible position and force combinations were simulated for one-point contact; 3600 trials were synthesized as a result. The two-point contact cases were randomly selected from the grid points. The amount of force in each grid point was also randomly modulated. As a result, 32 400 trials were synthesized for the two-point case.

Separately, another dataset was synthesized for the de-noising network. This dataset was obtained by simulating the identical indentation condition of the real experiment, in which each grid point was pressed until 4 mm indentation depth with eight intervals. Because our indenter has only one end-effector, we did not record real two-point contact data. Alternatively, we took data from simulated two-point contact and added Gaussian noise modeled from the real one-point contact data. In total, a dataset with 2124 trials (324 one-point contacts from reality + 1800 two-point contacts from simulation) was generated for learning the gap between real and simulation.

C. Training Procedure

All the training was conducted with the adaptive moment estimation (ADAM) optimizer [29]. The mini-batch was set to 32 to effectively generalize the training [30]. All trials were divided into a training set and a validation set with a ratio of 0.85 to 0.15. The training proceeded until convergence or 100 epochs.

D. Evaluation

To evaluate the calibration framework, we created a test dataset from the real sensor. It should be noted that the test set was not included in the training or validation sets. Moreover, the test set was generated with an indentation experiment with different depths. The one-point contact test set was obtained from the XYZ stage over 36 grid locations with 8 different indentation depths. The two-point contact test set was manually conducted over 14 cases using two 500 g weights.

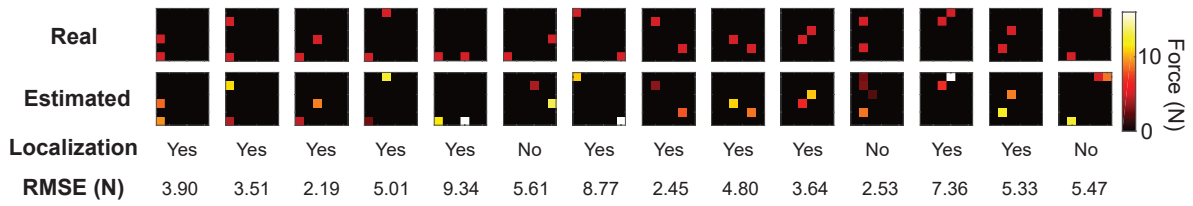


Fig. 11. Two-point contact test results for 14 sample trials.

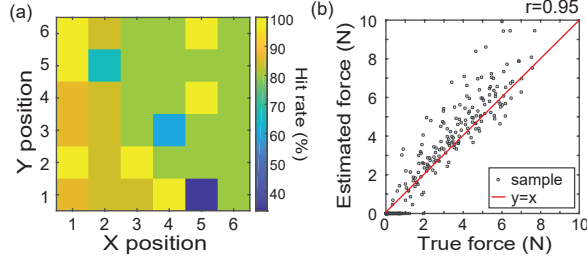


Fig. 10. Results of the single-point test showing (a) localization performance and (b) force estimation.

Fig. 10 (a) shows the result of the localization performance of the single-point contact test. The hit rate was calculated using the reference and estimated contact locations. The average hit rate was $82 \pm 12\%$. The localization performance was slightly higher on the left side of the sensor than the right side. This difference could be caused by a mechanical asymmetry in the test setup, which results in higher contact force and larger voltage changes on the left side for the same commanded indentation depth.

Fig. 10 (b) presents the force estimation performance. Due to the threshold layer in the DNN model, forces lower than 1 N are mostly suppressed. The correlation between the estimation and true force is 0.95. In general, ERT-based tactile sensors show poor force estimation performance due to their nonlinear characteristics [6]. The RMSE between estimated and true force was 0.51 ± 0.72 N, which is nearly 6% of the maximum force.

The two-point contact results appear in Fig. 11. The results show that the DNN model successfully localized both contacts with no false positives or negatives in 11 of the 14 tested cases (78.5%). The force estimation error for two-point contact was 5.0 ± 2.2 N on average. Although force estimation performance is not as accurate as single-contact test, it should be noted that this DNN model was trained without any real two-point contact data.

V. DISCUSSION AND CONCLUSIONS

This paper introduced a calibration method for ERT-based tactile sensors. The proposed method blends a model-based approach with a data-driven approach. Data-driven approaches generally require a large amount of data, which is physically difficult to acquire for large-scale tactile sensors. We hypothesized that a multiphysics model of an ERT-based tactile sensor can resolve this data deficiency problem using sim-to-real transfer learning.

We constructed a simple multiphysics model that maps contact pressure to voltage measurements. The model was

optimized to estimate voltage measurements close to the real voltage measurements. We tried to balance model complexity with computational cost, obtaining a lightweight model that largely follows the trends of the real system; nonlinear elasticity, inhomogeneous piezoresistivity, and sensor dynamics are most likely responsible for the remaining gap between our model and reality.

We introduced a new deep learning architecture that can capture the simulation-to-real gap and reconstruct applied contacts from voltage measurements. As a preliminary study, we divided the sensing area into a 6 by 6 grid and generated one- and two-contact datasets using the multiphysics model to train the DNN model. The results revealed that this method can estimate contact location and force well in the single-contact case. It also succeeded moderately well at generalizing from one contact to a two contact scenario that was not seen in the training dataset. It should be noted that the grid size used in this study is relatively small compared to conventional ERT-based tactile sensors [6]. The influence of the grid size needs to be investigated further to generalize the calibration method.

In the future, ERT-based tactile sensors can be applied to whole-body robotic skins for monitoring diverse contact situations. Extending this calibration framework for more complicated contact cases will require both accurate models and significant real data. Moreover, using supervised learning for calibrating a body-mounted tactile sensor will be challenging. Although the DNN model was tested only with one-point and two-point contacts, the proposed method showed remarkable performance for contact point localization and force estimation. This framework can be improved if real multi-contact data is included in training.

ACKNOWLEDGMENTS

This work was supported by the Max Planck Society, the National Research Foundation of South Korea (NRF-2018R1A6A3A03010897), and the China Scholarship Council. The authors would like to thank Jung Kim and Georg Martius for their substantial support, Kyungseo Park for the piezoresistive behavior test, and Bernard Javot for technical support.

REFERENCES

- [1] R. S. Dahiya, G. Metta, M. Valle, and G. Sandini, "Tactile sensing: from humans to humanoid," *IEEE Transactions on Robotics*, vol. 26, no. 1, pp. 1–20, 2010.
- [2] M. L. Hammock, A. Chortos, B. C.-K. Tee, J. B.-H. Tok, and Z. Bao, "25th anniversary article: The evolution of electronic skin (e-skin): A brief history, design considerations, and recent progress," *Advanced Materials*, vol. 25, no. 42, pp. 5997–6038, 2013.

- [3] C. Bartolozzi, L. Natale, F. Nori, and G. Metta, "Robots with a sense of touch," *Nature Materials*, vol. 15, no. 9, p. 921, 2016.
- [4] H. Lee, D. Kwon, H. Cho, I. Park, and J. Kim, "Soft nanocomposite based multi-point, multi-directional strain mapping sensor using anisotropic electrical impedance tomography," *Scientific Reports*, vol. 7, 2017.
- [5] H. Lee, K. Park, J. Kim, and K. J. Kuchenbecker, "Internal array electrodes improve the spatial resolution of soft tactile sensors based on electrical resistance tomography," in *Proceedings of the IEEE International Conference on Robotics and Automation (ICRA)*, Montreal, Canada, 2019, pp. 5411–5417.
- [6] D. Silvera-Tawil, D. Rye, M. Soleimani, and M. Velonaki, "Electrical impedance tomography for artificial sensitive robotic skin: a review," *IEEE Sensors Journal*, vol. 15, no. 4, pp. 2001–2016, 2015.
- [7] D. Silvera-Tawil, D. Rye, and M. Velonaki, "Interpretation of the modality of touch on an artificial arm covered with an EIT-based sensitive skin," *The International Journal of Robotics Research*, vol. 31, no. 13, pp. 1627–1641, 2012.
- [8] F. Visentin, P. Fiorini, and K. Suzuki, "A deformable smart skin for continuous sensing based on electrical impedance tomography," *Sensors*, vol. 16, no. 11, p. 1928, 2016.
- [9] A. Yao, C. L. Yang, J. K. Seo, and M. Soleimani, "EIT-based fabric pressure sensing," *Computational and Mathematical Methods in Medicine*, 2013.
- [10] H. Lee, K. Park, Y. Kim, and J. Kim, "Durable and repairable soft tactile skin for physical human robot interaction," in *Companion Proceedings of the International Conference on Human-Robot Interaction (HRI)*, 2017, pp. 183–184.
- [11] D. S. Holder, *Electrical Impedance Tomography: Methods, History and Applications*. CRC Press, 2004.
- [12] V. Chitturi and F. Nagi, "Spatial resolution in electrical impedance tomography: A topical review," *Journal of Electrical Bioimpedance*, vol. 8, no. 1, pp. 66–78, 2017.
- [13] S. Martin and C. T. Choi, "Nonlinear electrical impedance tomography reconstruction using artificial neural networks and particle swarm optimization," *IEEE Transactions on Magnetics*, vol. 52, no. 3, pp. 1–4, 2015.
- [14] H. Park, H. Lee, K. Park, S. Mo, and J. Kim, "Deep neural network approach in electrical impedance tomography-based real-time soft tactile sensor," in *Proceedings of the IEEE/RSJ International Conference on Intelligent Robots and Systems (IROS)*, pp. 7447–7452, 2019.
- [15] A. Molchanov, O. Kroemer, Z. Su, and G. S. Sukhatme, "Contact localization on grasped objects using tactile sensing," in *Proceedings of the IEEE/RSJ International Conference on Intelligent Robots and Systems (IROS)*, Oct 2016, pp. 216–222.
- [16] L. Zou, C. Ge, Z. J. Wang, E. Cretu, and X. Li, "Novel tactile sensor technology and smart tactile sensing systems: A review," *Sensors*, vol. 17, no. 11, 2017.
- [17] H. Sun and G. Martius, "Machine learning for haptics: inferring multi-contact stimulation from sparse sensor configuration," *Frontiers in Neurobotics*, vol. 13, p. 51, 2019.
- [18] S. Russo, R. Assaf, N. Carbonaro, and A. Tognetti, "Touch position detection in electrical tomography tactile sensors through quadratic classifier," *IEEE Sensors Journal*, vol. 19, no. 2, pp. 474–483, 2018.
- [19] M. E. Taylor and P. Stone, "Transfer learning for reinforcement learning domains: A survey," *Journal of Machine Learning Research*, vol. 10, no. Jul, pp. 1633–1685, 2009.
- [20] J. Tobin, R. Fong, A. Ray, J. Schneider, W. Zaremba, and P. Abbeel, "Domain randomization for transferring deep neural networks from simulation to the real world," in *Proceedings of the IEEE/RSJ International Conference on Intelligent Robots and Systems (IROS)*, 2017, pp. 23–30.
- [21] K.-S. Sohn, J. Chung, M.-Y. Cho, S. Timilsina, W. B. Park, M. Pyo, N. Shin, K. Sohn, and J. S. Kim, "An extremely simple macroscale electronic skin realized by deep machine learning," *Scientific Reports*, vol. 7, no. 1, p. 11061, 2017.
- [22] G.-R. Liu and S. S. Quek, *The finite element method: a practical course*. Butterworth-Heinemann, 2013.
- [23] G. N. Greaves, A. Greer, R. S. Lakes, and T. Rouxel, "Poisson's ratio and modern materials," *Nature Materials*, vol. 10, no. 11, p. 823, 2011.
- [24] Z. Jinyun, L. Yi, J. Lam, and C. Xuyong, "The Poisson ratio and modulus of elastic knitted fabrics," *Textile Research Journal*, vol. 80, no. 18, pp. 1965–1969, 2010.
- [25] B. Ellis and R. Smith, *Polymers: a property database*. CRC Press, 2008.
- [26] P. Vincent, H. Larochelle, Y. Bengio, and P.-A. Manzagol, "Extracting and composing robust features with denoising autoencoders," in *Proceedings of the International Conference on Machine Learning (ICML)*, 2008, pp. 1096–1103.
- [27] E. Alpaydin, *Introduction to Machine Learning*. MIT press, 2009.
- [28] V. Nair and G. E. Hinton, "Rectified linear units improve restricted boltzmann machines," in *Proceedings of the international conference on machine learning (ICML)*, 2010, pp. 807–814.
- [29] D. P. Kingma and J. Ba, "ADAM: A method for stochastic optimization," *arXiv preprint arXiv:1412.6980*, 2014.
- [30] D. Masters and C. Luschi, "Revisiting small batch training for deep neural networks," *arXiv preprint arXiv:1804.07612*, 2018.